

Article

Wear Analysis of Friction Stir Processed AA7075-SiC-Graphite Hybrid Surface Composites

Namdev Ashok Patil ¹, Srinivasa Rao Pedapati ^{2,*}  and Roshan Vijay Marode ² ¹ Department of Mechanical Engineering, JSPM's Rajarshi Shahu College of Engineering, Pune 411033, India² Department of Mechanical Engineering, Universiti Teknologi PETRONAS, Seri Iskandar 32610, Malaysia* Correspondence: srinivasa.pedapati@utp.edu.my; Tel.: +60-111-516-6816

Abstract: High specific strength and superior corrosion resistance are two key characteristics of the aerospace grade AA7075-T6 alloy. However, the surface behavior of AA7075-T6 is found to be deprived, because of its behavior of being prone to fretting fatigue and adhesive wear under dry sliding conditions. Thus, surface wear behavior improvement with the retention of the microhardness of the alloy is required for increasing its wider application. For this, surface isomorphous precipitates and the soft matrix need to be protected through dispersion of hard thermally stable ceramic SiC with solid-lubricant graphite particles. The dispersion through friction stir processing (FSP) avoids detrimental phase formations by processing the metal alloy below its melting point temperature. Thus, dispersion of SiC-Graphite inside the AA7075-T6 using FSP is the focal point of the study. The low and high wear rate samples have been analyzed using SEM imaging and elemental analysis through XRD and EDS mapping. In this study, reinforcing the SiC-Gr particles greatly improved the wear behavior of the AA7075 alloy. Wear resistance has been controlled by combining soft solid lubricant Gr particles with load-bearing hard SiC nanoparticles. In dry sliding action, the base alloy matrix was severely exposed to wear, but the hard SiC nanoparticles served as load-bearing asperities and improved the wear resistance. Simultaneously, the graphite layers generated the soft solid lubricating tribofilm further to reduce the wear and friction between mating surfaces. The wear mechanisms have changed prominently from adhesion to abrasion and delamination through reinforcing the SiC-Gr reinforcements. The graphite content in a hybrid ratio with SiC hard particles was found to have improved the wear resistance by 78%. The tendency of fatigue was more effectively improved in surface composites as compared to the base alloy.

Keywords: AA7075-T6; wear; adhesion; graphite; silicon carbide

Citation: Patil, N.A.; Pedapati, S.R.; Marode, R.V. Wear Analysis of Friction Stir Processed AA7075-SiC-Graphite Hybrid Surface Composites. *Lubricants* **2022**, *10*, 267. <https://doi.org/10.3390/lubricants10100267>

Received: 12 September 2022

Accepted: 10 October 2022

Published: 18 October 2022

Publisher's Note: MDPI stays neutral with regard to jurisdictional claims in published maps and institutional affiliations.



Copyright: © 2022 by the authors. Licensee MDPI, Basel, Switzerland. This article is an open access article distributed under the terms and conditions of the Creative Commons Attribution (CC BY) license (<https://creativecommons.org/licenses/by/4.0/>).

1. Introduction

The low density, high specific strength, and excellent corrosion resistance of the 7xxx family of aluminum alloys make them very popular for wider applications. They are being used more and more for lightweight structural components in the automotive and aerospace sectors, where weight reduction is important in minimizing fuel consumption and exhaust emissions [1]. The goal of the design engineers is to create strong, lightweight materials for structural purposes. Due to their excellent characteristics, aluminum alloys are displacing steel alloys in a variety of applications [2,3]. However, their broader applicability is being limited by weak surface characteristics including wear resistance under high load applications. Because the martensitic phase is absent, Al alloys cannot be significantly hardened by induction hardening as steels may be. Due to the “thin-ice effect,” thin hard coatings do not last over aluminum alloys in heavy stress situations [4].

Production of bulk and surface metal matrix composites (MMCs) has increased in popularity over the past three decades. The MMC approach's key promise is its capacity to provide specific reinforcements and hence generate tailored features [5]. To create metal matrix hybrid composites, two or more reinforcements must now be deposited into metal

alloys. This approach has opened up a number of opportunities for the production of low-cost, high-performance materials with the ability to adjust their specific characteristics.

Surface MMCs have been synthesized in the area of surface engineering utilizing a variety of techniques, including cast sintering, plasma spraying, laser melting, cold spraying, stir casting, and the electron beam irradiation method, etc. [6–15]. Due to processing at temperatures over the melting points of the corresponding metal alloys, these production methods have shown several shortcomings. Processing temperatures generate problems such as particle agglomeration, unfavorable phase development, porosity, slack interfacial bonding, and, most significantly, interfacial reactions. The production of unanticipated reaction products within the composites is caused by processing above the melting point. For many surface features, the production of inevitable harmful phases becomes necessary. Due to the drawbacks of the aforementioned methodologies, it is now more important than ever to identify a reliable replacement strategy for the synthesis of MMCs. In order to create superplasticity in the AA7075 alloy, R.S. Mishra and colleagues developed the FSP process in 1999 [16]. Recently, FSP has become a more adaptable practice for producing surface composites. The Al-SiC-Gr functionally graded composites were developed and it has been confirmed that the failure stress was higher for composites with higher content of SiC. The hardness increased significantly due to higher SiC content in the upper layer [17]. The AA7075-T651-SiC composites fabricated using friction stir processing and the average hardness obtained increased more than the parent metal [18]. The AA6063-SiC-Gr composites synthesized using friction stir processing showed increased microhardness for the more SiC reinforced composites [19]. Moreover, the friction stir processed Al6061-SiC-graphite composites showed significant increase in the mechanical properties than the base alloy. The axial forces variation was observed due to graphite flakes having higher thermal conductivity [20]. The Al6061 composites reinforced with carbon nano tubes, graphene nanoplates and graphite particles were fabricated using friction stir processing. The wear rate has decreased significantly in cases of graphene exfoliation into a few layers. The surface area covered was more inside the composites by the exfoliated graphene layers and thus the wear resistance increased significantly [21].

The AA7075 alloy is primarily employed in structural applications in the automotive and aerospace industries, because of its high specific strength and strong resistance to stress corrosion cracking, [22–24]. Under situations of surface-to-surface loading, they have inadequate surface characteristics. Under surface cyclic stress circumstances, the AA 7075 has shown three behaviors: fretting fatigue and adhesive wear susceptibility, limited fatigue performance, low toughness, and environment-sensitive fracture in service. The isomorphous $MgZn_2$ precipitates are the main reinforcing phases inside the AA7075 alloy. However, during the cyclic surface loading conditions, due to frictional heating of the contacting surfaces, over-aged precipitates zones are formed. Therefore, the resultant coarsening in the strengthening precipitates occurs within the aluminum (FCC) matrix. Furthermore, it leads to matrix softening due to the coarsened weak precipitates' presence over the surface. With the $MgZn_2$ precipitates from the solute-rich solid solution become coarser, the matrix's mechanical characteristics become less robust. Therefore, hard debris and separated particles from the mating surfaces readily weaken a soft and low-strength matrix on the surface with coarse precipitates. These removed and impaired functioning hard debris fragments under cyclic stresses also cause harmful brittle oxide phase forms [25–28]. The presence of oxide phase formations in the hard debris particles confirms the fretting fatigue and adhesive wear mechanisms. Thus, the surface of the AA7075 alloy needs to be dispersed with the hard, thermally and mechanically stable synthetic ceramic particles to protect the soft matrix and isomorphous precipitates from detrimental oxide formations and coarsening, respectively. Also important to note that in the current study fabrication of the AA7075-surface hybrid composites with reinforcing the silicon carbide (SiC) along with the solid lubricant graphite (Gr) flakes has been conducted. This approach through ex-situ composite fabrication is to be utilized in order to make the surfaces more resistant to wear under cyclic dry sliding surface loading conditions. Nevertheless, no research

on the impact of encapsulating SiC and graphite nanopowders with various FSP process conditions within the base alloy on surface attributes has been published. Thus, the effects of graphite exfoliation through super plastic deformation over the mitigation of fretting and fatigue crack nucleation is investigated and discussed in detail.

2. Materials and Methods

The basic metal utilized was the rolled AA 7075-T651 aluminum alloy specimens with sizes of 110 mm × 150 mm and thickness of 6.35 mm. In Table 1, the chemical composition of Al 7075-T651 is shown.

Table 1. Chemical composition of Al 7075-T651 alloy.

Component	Al	Zn	Mg	Cu	Fe	Si	Ti	Cr	Mn	Other
Weight%	87.1–91.4	5.1–6.1	2.1–2.9	1.2–2	0.5	0.4	0.2	0.18–0.28	0.3	0.15

2.1. Silicon Carbide

The SiC powder with an average particles size of 1.1 μm has been used. The particles' morphology is observed to be cylindrical rods/needles and elongated cubic structures. The SiC composition type is 3C beta (β) cubic crystal structure polytype. This type of SiC particles has a greater surface area compared to alpha hexagonal polytype particles.

2.2. Graphite Nanoflakes

As reinforcements, graphite (Gr) flakes with widths between 4 and 6 μm and thicknesses under 40 nm are employed. Scanning electron microscopy (SEM) imaging is used to validate the shape and sizes of the Gr flakes. The Gr flakes are 99% pure and charcoal dark black in color. The thermally stable, chemically inert, soft, lightweight graphite flakes are utilized mainly for improving the wear behavior of the composites. These graphite flakes are made up of multiple layers of graphene nanosheets. The overall morphology of the flakes was observed to be like thin, layered sheets.

2.3. Composites Fabrication

The reinforcing particles are preplaced over the surface of the base alloy using the surface blind holes technique as shown in Figure 1. Using hand compaction, the reinforcing powder was compacted into the surface blind holes. To guarantee optimal distribution throughout the FSP process, the reinforcement powder mixture must completely fill the hole. Here are the specifications of the procedure: The alloy plate was then fastened over the machine table utilizing fixtures configurations. The tool for capping H13 steel that excludes pins has been used. The tool holder on the rotatable spindle must be secured with the capping tool inside. All composites have undergone capping passes at w-1000 rpm, v-30 mm/min, and 0.3 mm of tool plunge depth. Following capping, the cavities fully packed with reinforcements inside have been sealed with a thin layer of the base alloy.

For each composite band, a single FSP pass was used to perform the composite plates. The AA7075-T6 plate, which has been securely fastened, covers the workbench surface. This is carried out to avoid losing the plate during the FSP run. The H13 steel tool with a straight cylindrical profile is then placed on top of the plate that is being clamped. In accordance with the run parameters recommended by the L27 matrix [29] of the response surface central composite design, and with the tool rotational speed (500, 1000 and 1500 rpm) and tool traverse speed (20, 30 and 40 mm/min), the SiC-Graphite hybrid ratio (60:40, 75:25 and 90:10) and SiC-Graphite volume percentage (4, 8 and 12%) as input independent parameters, the 27 surface composites were fabricated.

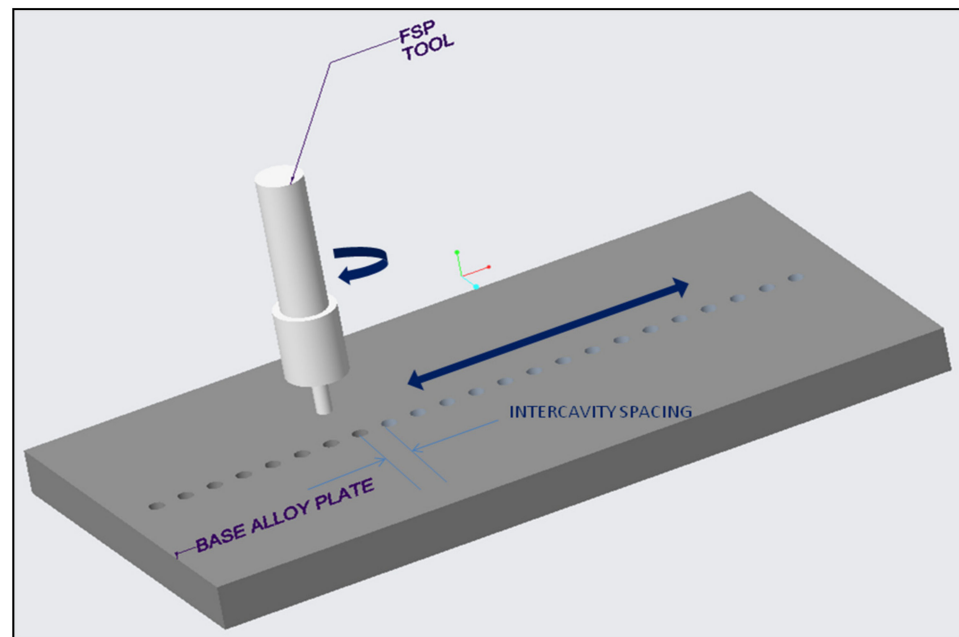


Figure 1. Schematics of Friction Stir Processing.

The other parameters such as tool tilt angle (TT) of 2.5° , axial load of 10 kN, and 10 s dwell, have been held constant for all samples in the FSP process. For a 2.5° TT, the recommended tool plunge depth is 5.3 mm where the macro level flaws, such as wormholes, tunnels, and voids, have been effectively eliminated [30]. The FSP tool used has the pin length 4.5 mm with a diameter of 6 mm, and shoulder diameter of 20 mm with flat cylindrical configuration of the pin profile. The surface blind holes are of a depth of 4 mm and a diameter of 2 mm with intercavity spacing of 4 mm, 6 mm and 8 mm, respectively. The wear samples have been cut from the middle of the band.

2.4. Wear Characterization

For testing the wear behavior, the pin-on-disc arrangement is utilized. The composite material's pin has been conceded against mating mild steel disc under normal loading conditions. According to ASTM-G99-17 standards [31], the wear samples are sized: 10 mm in length and width, and thickness of 6 mm have been taken using a wire EDM machine from the center of each composite's stir zone (SZ). The samples after cutting have been surface finished with 800-grit SiC paper in order to make its surface roughness equivalent to the mating disc. The sample surfaces have been cleaned with acetone before conducting the tests.

The disc in the pin-on-disc arrangement consists of mild steel disc material. The pin-on-disc equipment used in these tests is Tribology Trainer Module- TM 260 manufactured by Gunt Humburg. Following testing of each of the 27 specimens, wear loss has been calculated for each sample. The weight difference between the wear sample's before- and after-test weight is used to quantify wear loss. Weight balances with the lowest count of 0.1 mg are used to measure weights. Each sample was operated for 20 min at 150 rpm while being loaded with 20 N.

SEM imaging, energy dispersive x-ray analysis, and elemental mapping analysis have all been applied to the wear tracks of samples with the highest and lowest wear rates of each combination. Through the examination of SEM micrographs of worn-out surfaces, the potential wear processes that may be present and in charge of regulating the wear loss have been investigated. The wear track results and wear debris analysis of the same samples have been correlated. The possible wear mechanisms activated over the wear pin sample surface have been investigated. The wear debris' type, morphology of particles, the

presence of reinforcement particulates, oxides films, and mating material particles are the main aspects to be analyzed.

3. Results and Discussion

3.1. Microstructure of AA7075-SiC/Gr Composites

In the present study, a total of 27 SiC/Gr surface composites samples (S1–S27) were fabricated as per the response surface central composite design using Design Expert 10. The 27 samples processed with designed parameters and their microhardness and wear rates have been reported. Amongst these 27, the S-24 sample (processed at rotational speed-500rpm, traverse speed-20 mm/min, hybrid ratio of SiC/Graphite-60:40, volume percentage-12) and S-10 (processed at rotational speed-1500 rpm, traverse speed-40 mm/min, hybrid ratio of SiC/Graphite-60:40 and volume percentage-4), hybrid composites showed the highest (0.05175 mg/m) and lowest wear rate (0.01194 mg/m), respectively. Samples were cut and examined in this work for further microstructure investigation. The microstructure samples were prepared, and after etching, the imaging of the processed zone carried out using OM and SEM.

The micrographs obtained are observed carefully to understand the SiC/Gr nanoparticles' distribution, the movement of particles with plasticized metal during the processing, and the dispersion regions with low, medium, and highly dense SiC/Gr particles presence. The morphology of the AA7075-SiC-graphite composites has been shown in Figure 2. The onion rings on the surface composites are observed. Three composite bands were produced for every run of L27 combinations. The wear sample was cut from the middle of the band as shown in Figure 2. The Figures 3 and 4 show the optical imaging micrographs of run S-10 and run S-24 surface composite's stir zone region. From the optical micrographs, it is observed that the SiC/Gr nanoparticles' distribution inside the stir zone is governed by the resultant plasticized material movement during processing. Thus, bands with various particle presences are seen in the SZ areas. For S-10 composite, Figure 3a denotes the SiC-Gr particles moderate agglomeration in reverse s-shape area, and in other regions, it looks well distributed. Similarly, the SiC/Gr particles' distribution looks good and homogenous, as presented in Figure 3b–d. The S-10 composite band has been produced for the volume percentage of 4% and with the speed of 1500 rpm. Due to the high rotating speed, the SiC/Gr particles are now mainly uniformly spread with a few small dense clusters. The re-fined equiaxial fine grains' structure is a result of the grain size refinement, which was caused by the uniform distribution of SiC/Gr particles.



Figure 2. Friction Stir Processed Al7075-SiC-Graphite composites.

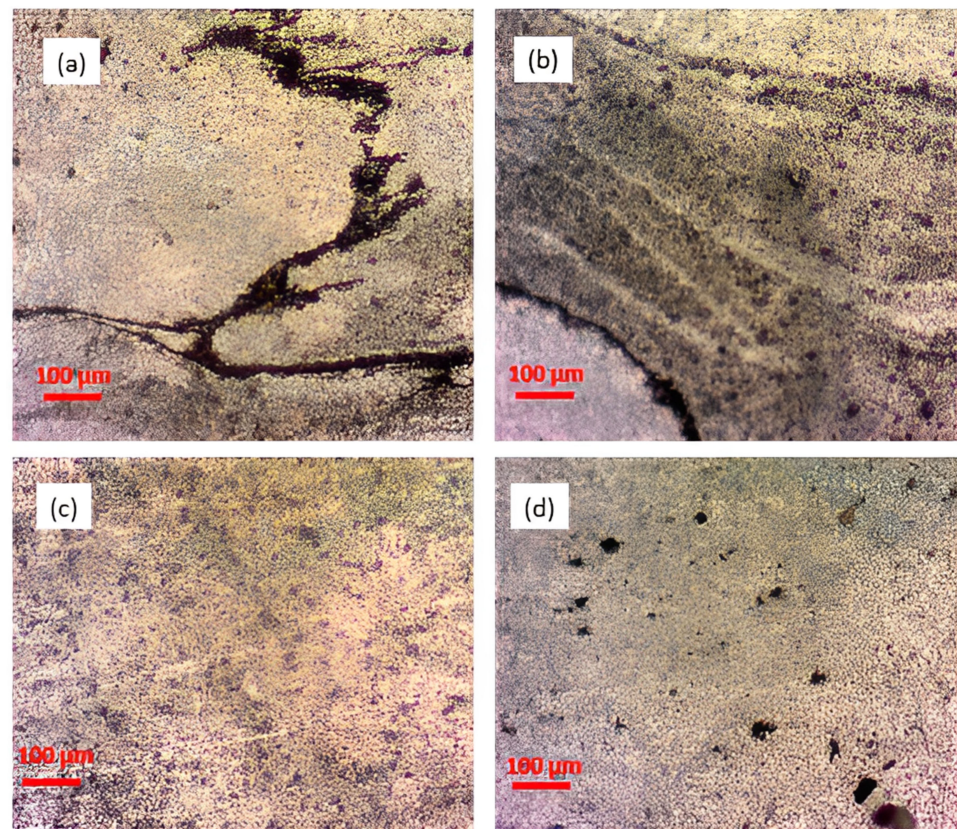


Figure 3. Optical microscopy images of S-10 AA7075-SiC/Gr stir zone.

Figure 4 depicts the particle distribution within the composite's stir zone after processing in the case of the S-24 composite. When compared to the S-10 composite, it has been shown that the particles are more densely distributed inside the aluminum matrix. The dense clusters of SiC/Gr particles have led to the porosity around the agglomerates, as shown in Figure 4b. The highly dense regions are observed in Figure 4a,c,d images. Here, in the S-24 composite, the tool rotational speed used is 500 rpm at 20 mm/min traverse for the volume percentage of 12% SiC/Gr. Thus, the extent of plastic deformation during the processing was not enough to give particles homogenous distribution within the matrix. The flow stress of the basic aluminum alloy must be greatly exceeded by the level of plasticization; only then would the dispersion have occurred more evenly. The high-volume percentage of SiC/Gr mixture was found to be difficult to disperse uniformly within the matrix band with lower stirring rotational speed.

In the Figure 5, SEM micrographs of Al7075-SiC/Gr composites from the S-24 sample that have been enlarged to demonstrate the SiC/Graphite particle dispersion inside the base alloy. The composite's stir zone (SZ) area is shown by the macrographs in Figures 5a and 6a. The plasticized material in the FSP typically moves from the advancing side (AS) to the retreating side (RS). The highly dense particle agglomerated zones are seen in the macrograph as green oval shape outlines. Due to weak interfacial bonding with the base alloy under surface-to-surface stress conditions, these zones are possible locations where the particles might break away. The porosity is also shown by the particles over agglomerated zones as a drawback. Particle agglomerates cause the formation of spheroids, which serve as locations for porosity and loose interfacial bonding areas where particle detachment may occur during surface loading.

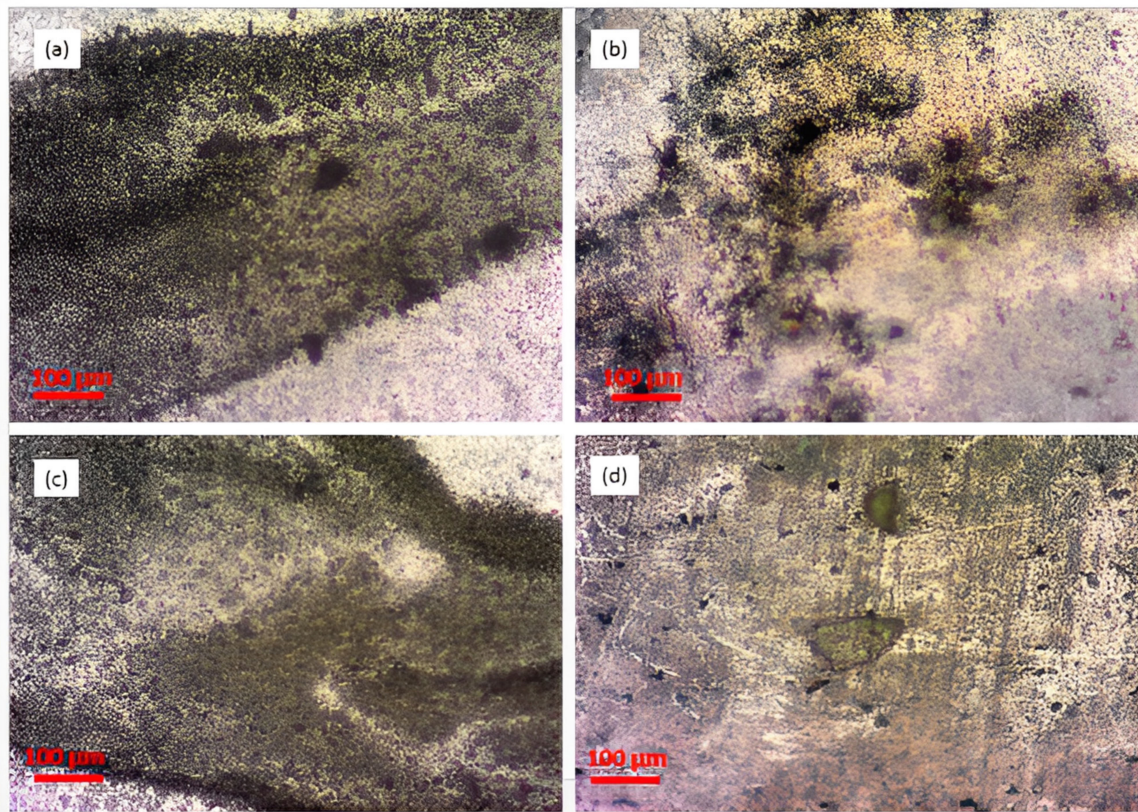


Figure 4. Optical microscopy images of S-24 AA7075-SiC/Gr stir zone.

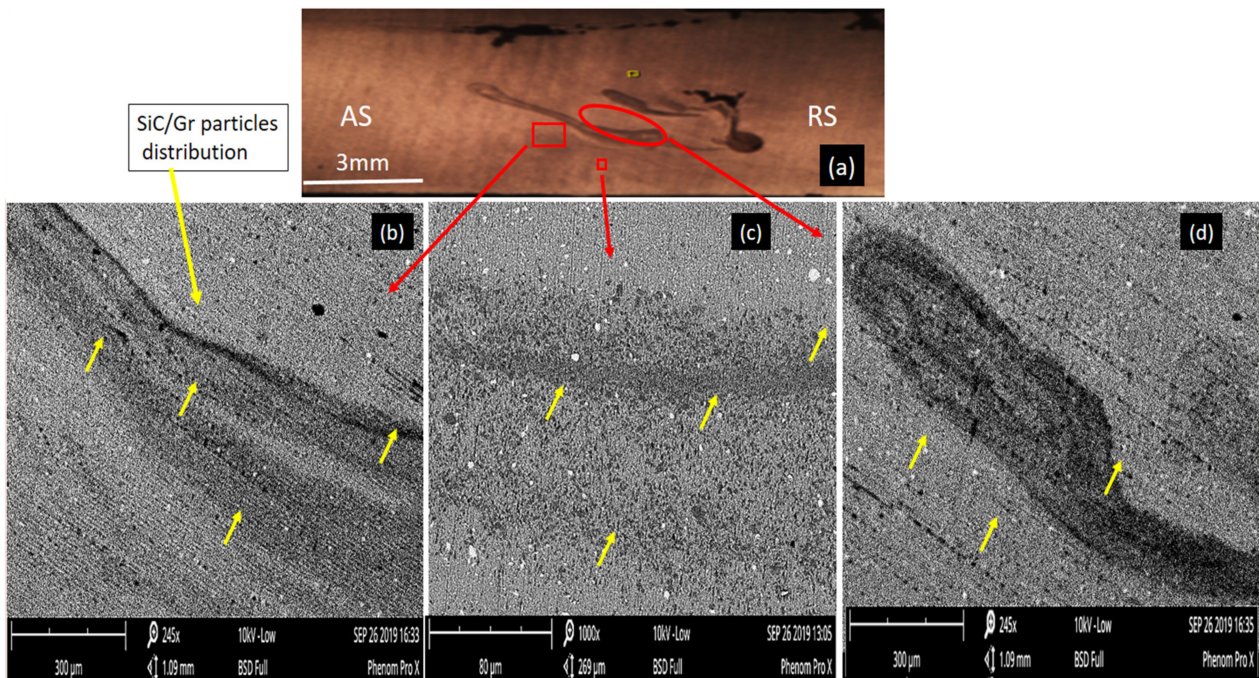


Figure 5. SEM micrographs of S-24 composite: (a) macrograph showing stir zone; (b) 245 \times ; (c) 1000 \times ; (d) 245 \times magnification micrographs denoting particles' distribution.

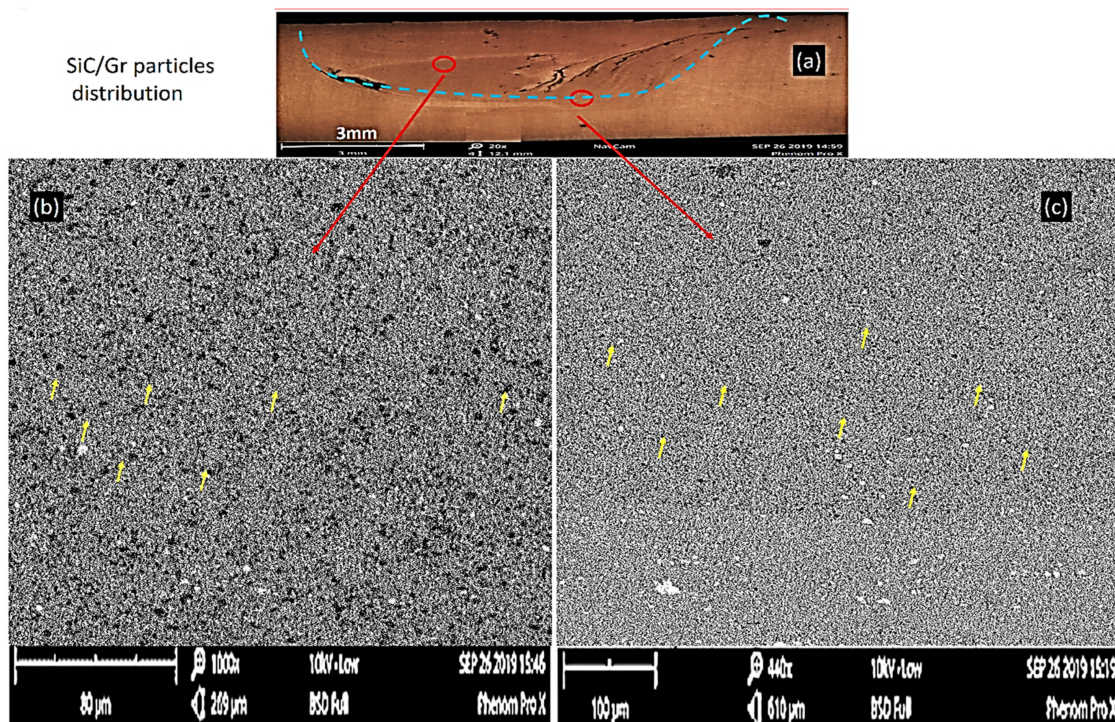


Figure 6. SEM micrographs of S-10 composite: (a) macrograph showing stir zone; (b) 1000 \times ; (c) 440 \times magnification micrographs denoting SiC/Gr particles' distribution.

The micrographs of Figure 5 show the variation in the SiC/Gr particles' dispersion within the stir zone. Due to the variable plasticized material movement during FSP, the resultant particle distribution varies in nature. Yellow arrow marks denote the particles clusters in the micrographs. It is observed that the material movement was prominent in the central part of the stir zone, however on the bottom side of retreating sides and advancing side's top portion, the material movement during plasticization was not enough to force the particles evenly in the composite band. It can be easily observed that the particles have moved from AS to RS and have gathered in the RS below half portion. At the top portion of the SZ, the forging action of the FSP tool was prominent to allow the generated intense plasticization to disperse the particles uniformly. Still, the material movement was not enough to get homogenous distribution on the lower side of the tool pin. Thus, the mismatch in the amount of SiC/Gr powder to be dispersed and the extent of plasticization that took place led to the agglomerated zones inside the composite.

For the S-10 composite, the SEM micrographs are shown in Figure 6, where the particle distribution within the band stir zone is observed. The macrograph of the processed zone depicts that the SiC/Gr reinforcement particles have distributed comparatively well in comparison to the S-24 composite. Only at the AS bottom, the small agglomerates are observed. On the retreating side, the particles agglomerations have not been regarded as like the S-24. The stirring action in the case of run S-10 was found to be intense enough to overcome the aluminum base alloy's flow stress and smoothed the particles' dispersion within the plasticized zones. Different areas on the bands have been observed using SEM, as shown in Figures 5 and 6, respectively. The yellow arrows indicate the SiC/Gr particles' dispersion agglomerates and continuous bands.

In both the composites of the S-10 and S-24, at the interface of the reinforced and unreinforced zones, the change in the microstructure has been observed. The reinforced zone indicates the presence of SiC hard particles with graphite nanosheets dispersed around and also the inherent insoluble constituent phases and soluble precipitates, whereas in the case of the unreinforced/particles free processed zone, the inherent isomorphous precipitates and insoluble constituent phases are present. The constituent phases are micron-

sized s, and an oval shape can be observed more clearly compared to the isomorphous phases in nanoscales. The presence of SiC-graphite particles has been confirmed through EDS and mapping analysis as shown in Figures 7 and 8, respectively.

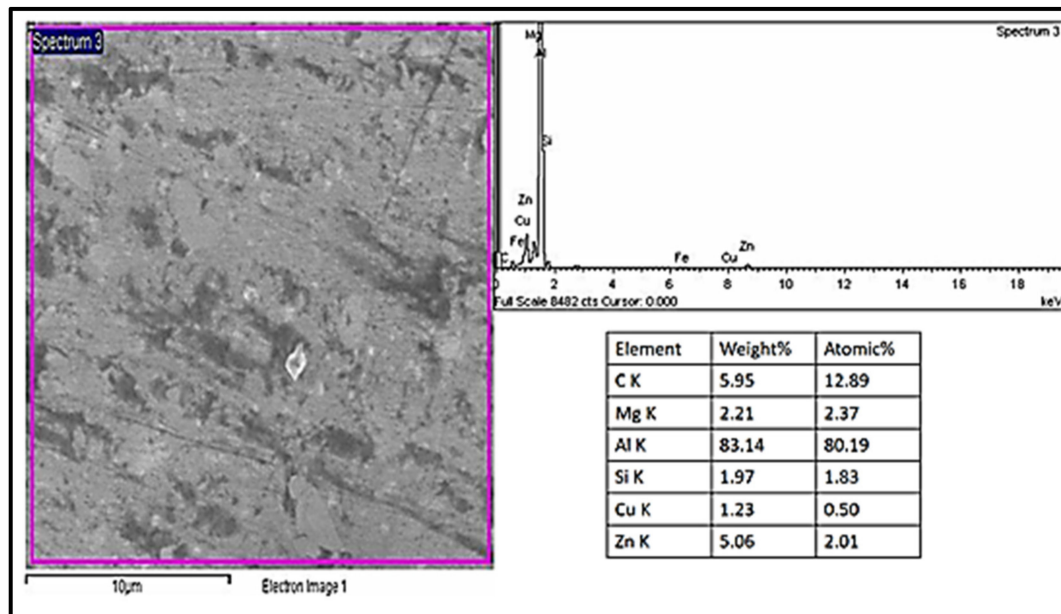


Figure 7. FESEM-EDX analysis of S-10 Al7075-SiC/Gr composite.

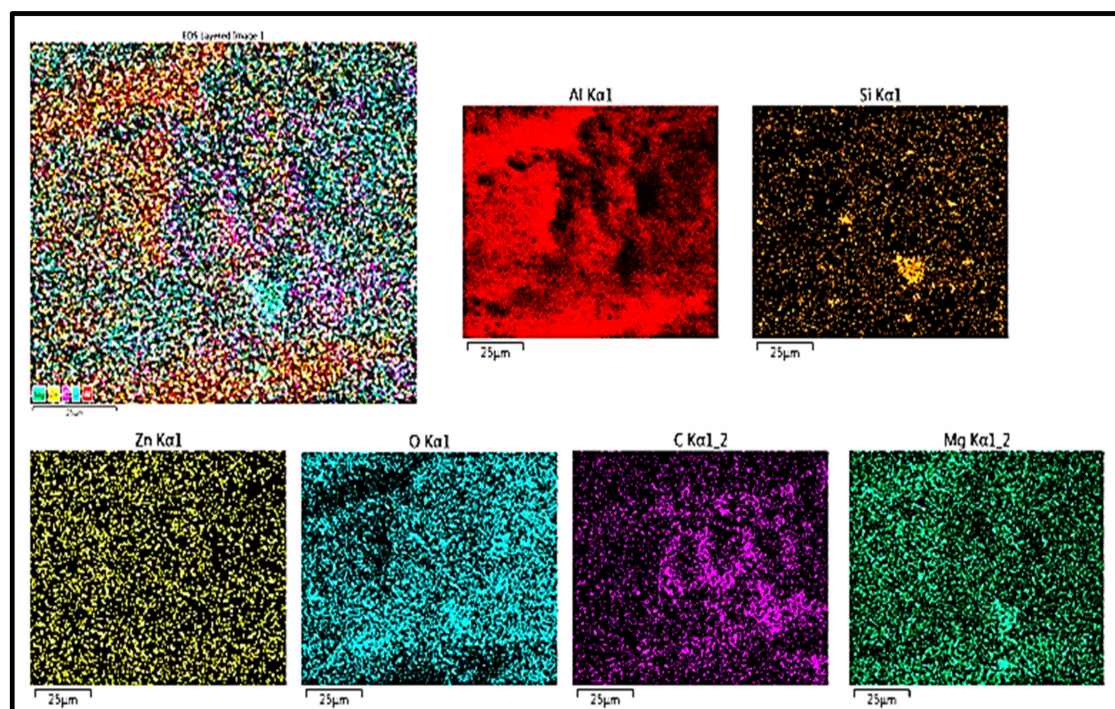


Figure 8. FESEM-Mapping analysis of S-10 Al7075-SiC/Gr composite.

Due to the very fast rotating, stirring action used in the S-10 composite, the SiC/Gr powders were well dispersed, and there was enough time to encapsulate the graphitic layers surrounding the SiC particles. The shear force during vigorous plasticization causes the graphite flakes to be exfoliated into multilayer graphene [32,33]. Due to the enormous surface area that graphite flakes naturally possess, they have a substantial coverage in the composites. Due to the severe plasticization, the SiC particles that break in both samples

have fractured into varying sizes. The base alloy and the SiC/Gr reinforcements are connected by the exfoliated graphitic layers, which have improved interfacial bonding. The hybrid ratio of graphite is limited to a maximum of 40% due to the material's very high heat conductivity, since amounts of Gr over this limit have caused tattering faults in the composite bands [33].

In contrast to the S-24 composite sample, the graphitized SiC particles in the S-10 sample are shown to have better interfacial bonding. Due to a more vigorous stirring action, the S-10 composite sample has more graphite layers encasing the SiC particles than the S-24 sample. The hybrid ratio of 60:40 is employed in both samples but run S-10's extreme plasticization caused by its fast-rotating speed made it easier to overcome the base alloy's flow stress, which led to an increase in the mobilization of particles within the matrix. The mobility and dispersion of the particles during the stirring action were constrained by the higher volume percentage (12%) of SiC/Gr powder and lower rotating speed (500 rpm) in S-24. On the other hand, the high rotating speed (1500 rpm) and low volume % of the SiC/Gr powder have enabled substantial particle mobility and dispersion in the matrix.

The Al 7075-SiC/Gr composites have a higher surface area covered by the very thin graphite flakes. The SiC particles have also been broken up and disseminated throughout the composites at the same time. The machine settings and reinforcement dispersion affected how the composite surfaces looked. The resulting grain size achieved within the composites has been impacted by the SiC/Gr reinforcement particles dispersion inside the matrix. Due to the presence of reinforcements, the pinning effect primarily regulates the grain development in treated composites. As a consequence, the resulting surface composites have a finer grain structure thanks to the encapsulation of reinforcements during severe plasticization. In the instance of the S-24 composite, it can be seen that the SiC/Gr particle interfaces suggest the potential for porosity surrounding them owing to poorer interfacial bonding.

It's confirmed that the S-10 composite surface contains SiC, Graphite, and ZnO inside the aluminum base alloy as shown in Figure 9. The base alloy Al shows peaks at $2\theta = 8.46^\circ$ with 100% match I% with [34]. The aluminum with cubic crystalline structure with indices (111) with an interlayer spacing of 2.3381 \AA is observed, matching with the base alloy results. The rhombohedral crystal structure for SiC has been observed at a peak of 35.621° , d-spacing 2.5183 \AA which matches 100% with the results from [35]. Many small peaks were present, indicating the SiC particles' presence with different intensities, e.g., at 60.047° at 73 I%, 37.84° at 73.4 I%, 38.48° at 56.9 I%, etc. with the same rhombohedral crystal structure with different Miller indices.

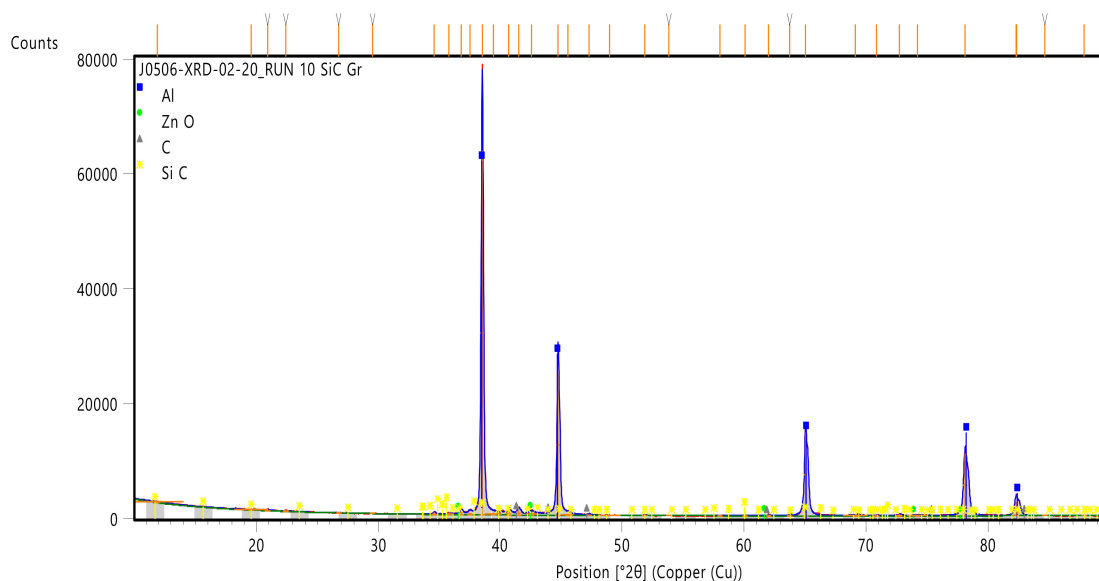


Figure 9. XRD results of S-10 AA7075- SiC/Gr surface composite.

The graphite content is indicated in terms of hexagonal crystal structured at 41.337° with (100) indices, which matches with the results in the system from [36]. The main graphite peak appears at 2θ of 26.5° . Like SiC, the graphite has also shown different intensity small peaks at various angles. The zinc oxide ZnO presence has also been confirmed in the analysis with the peak at 42.496° . The ZnO can be formed during processing by the reaction between the Zn in the form of precipitates with the atmospheric air. ZnO can also be observed between the surface-to-surface dry sliding actions as the isomorphous precipitates could react with the atmospheric oxygen to form the oxide film.

In S-24, the aluminum peak was observed at 38.508° with I%-100, with the cubic crystal structure (111) and interlayer d-spacing (2.335 \AA) minimally lowered compared to the S-10 composite, as shown in Figure 10. The SiC crystal structure was found to be hexagonal with a 36.222° peak with 100% intensity, d-spacing of 2.478 \AA , and other peaks with different intensities and miller indices. Here, the d-spacing of the SiC crystal structure looks lower than the S-10. The graphite with a hexagonal crystal structure shows the peak at 42.803° with 100.0 match intensity. The d-spacing again in this S-24 case is lower than the S-10 sample. The ZnO presence was again found with the d-spacing 2.125 , peak at 2θ angle of 42.496° . Thus, from the XRD results, the SiC/graphite embedding inside the composite is confirmed with some oxide layer formation on the surface.

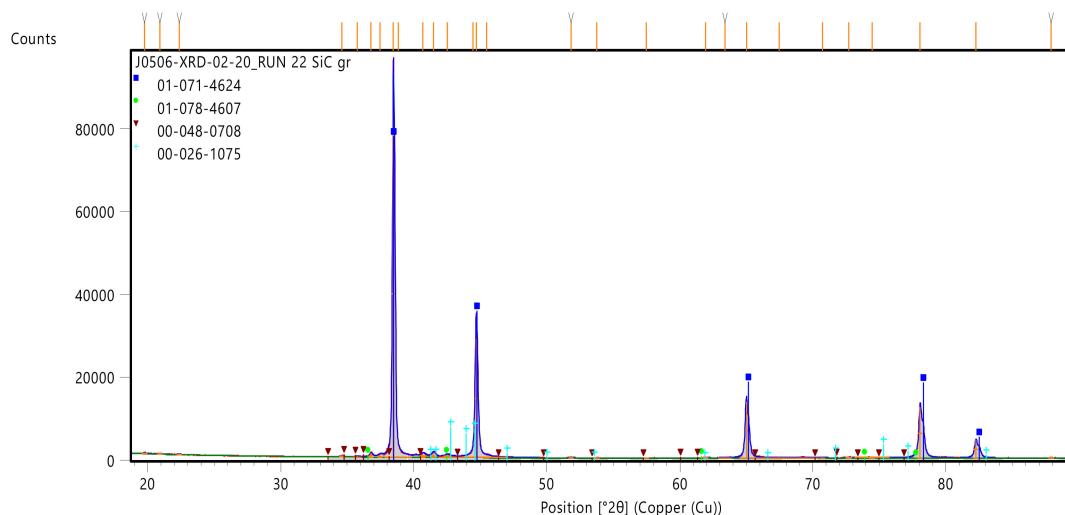


Figure 10. XRD results of S-24 AA7075-SiC/Gr surface composite.

3.2. Wear Properties of AA7075-SiC/Gr Composites

The wear rate in mg/m for all of the L27 runs are represented in the bar graph as shown in Figure 11. The wear resistance has improved overall for the Al 7075-SiC/Gr samples compared to the base alloy. Under dry sliding circumstances, the wear rates of the surface composites were calculated using a Pin-on-Disc tribometer. The results of the wear are encouraging and have shown the significant effect of embedding the hard SiC and soft solid lubricant graphite nanoflakes on the surface behavior of the composites under dry sliding conditions, with this being different to the fretting wear behavior of the base alloy.

3.2.1. Wear Tracks Analysis of AA7075-SiC/Gr Composites

Figures 12 and 13 show the wear tracks on the pins of base alloy AA7075-T6. The surface fatigue and resulting fretting wear taking place can be observed on the surface wear tracks. Mainly, the precipitates' dense zones have been found to be prone for the fretting fatigue wear nucleation sites. From the images of the tracks, it can be observed that the dark black colors are the inherent isomorphous precipitates and the constituent phases zones, upon which repeated cycling loading among the asperities of the mating materials start showing symptoms of the fatigue micro cracks, which then subsequently convert into the crater area of the loose debris. The debris particles pulled out again have

churned and acted as the abrasive medium between the mating materials, which led to the small abrasion lines. Along the parallel tracks of the dry sliding wear, tiny pits started to develop as a result of the adhesion caused by localized plastic flow, which was also seen on the surface. The adhesion and fretting fatigue wear were found to be prominent mechanisms responsible for the wear of the AA7075-T6 alloy samples.

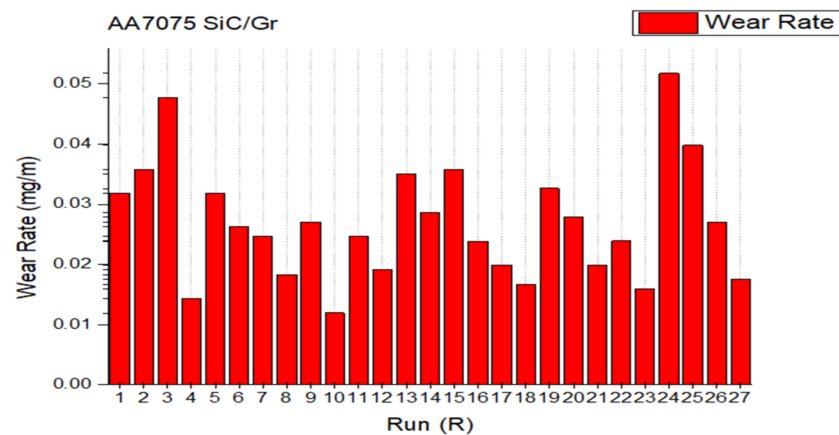


Figure 11. Wear rates of L27-AA7075-SiC-graphite composites.

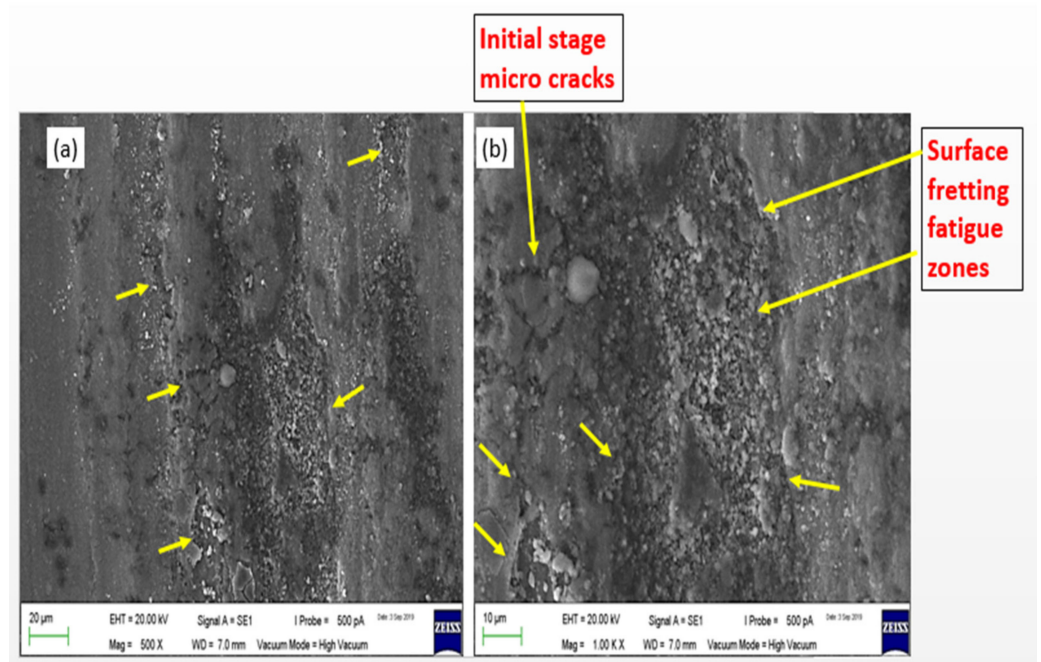


Figure 12. SEM micrographs of the wear tracks of AA7075-T651 base alloy (a) magnification 500 \times and (b) magnification 1000 \times .

For the S-10 composite, the wear tracks are as shown in Figures 14 and 15. The delamination, and fatigue tendency has been observed over the surface as shown in Figure 15. The EDX and mapping of the sample-area shown in Figure 14 are presented in Figures 16 and 17, respectively. Analysis of the S-10 composite's wear track has confirmed the existence of mating steel disc particles and SiC/Gr reinforcement particles. Figure 16 in the following text displays the SEM EDX analysis for such confirmation. The wear track has dark patches that are consistent with the graphitized SiC particles seen in spectrum77 in Figure 16. The presence of the most carbon (C) shows that the areas with SiC/Gr reinforcements are those.

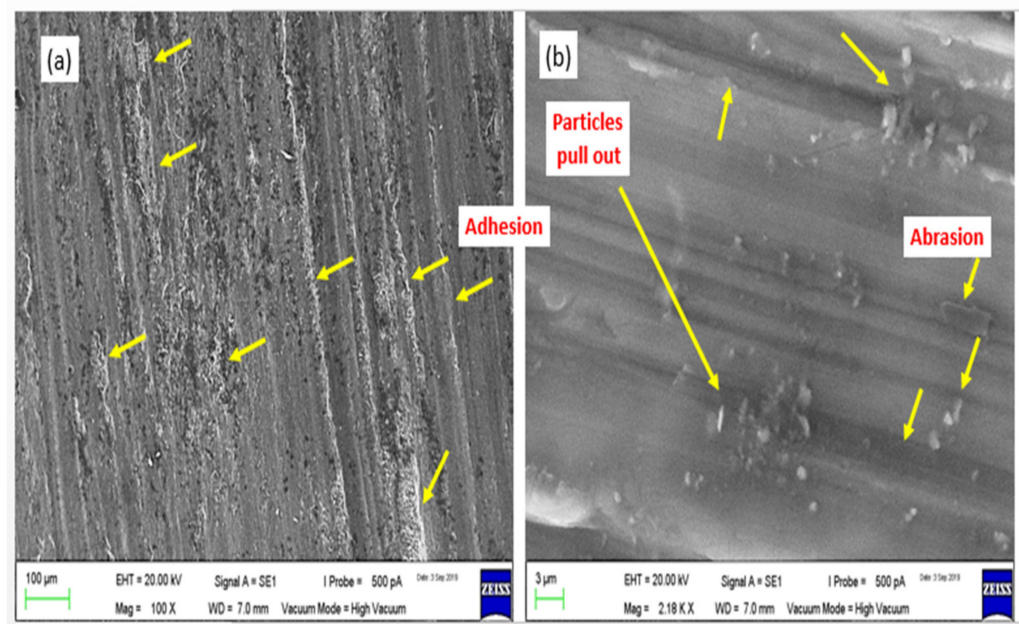


Figure 13. SEM micrographs of the wear tracks of AA7075-T651 base alloy: (a) magnification 100 \times and (b) magnification 2180 \times .

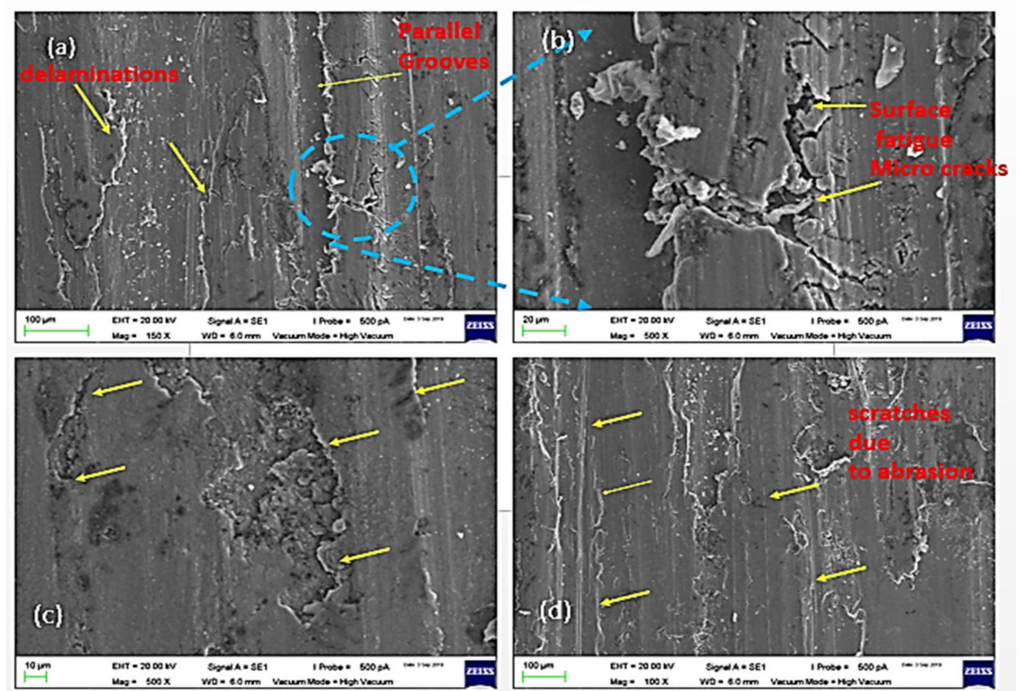


Figure 14. SEM micrographs of the wear tracks of AA7075-SiC/Gr S-10 composite with (a) magnification 100 \times and (b) magnification 500 \times (c) 100 \times and (d) 100 \times .

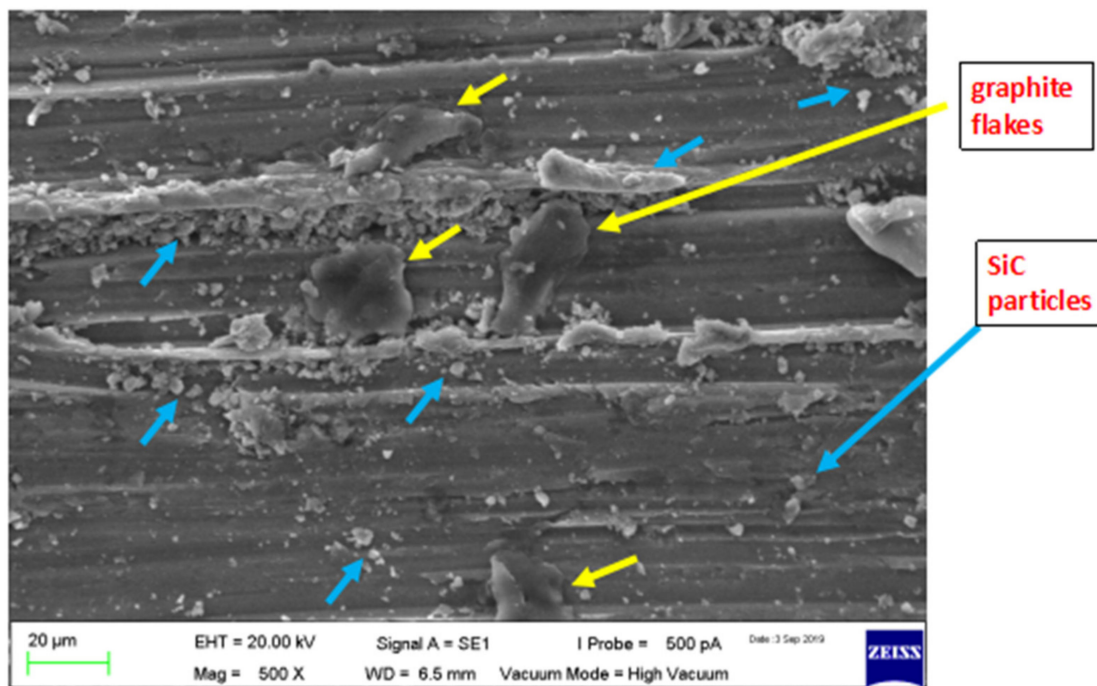


Figure 15. Wear track SEM micrograph of the S-10 AA7075-SiC/Gr sample.

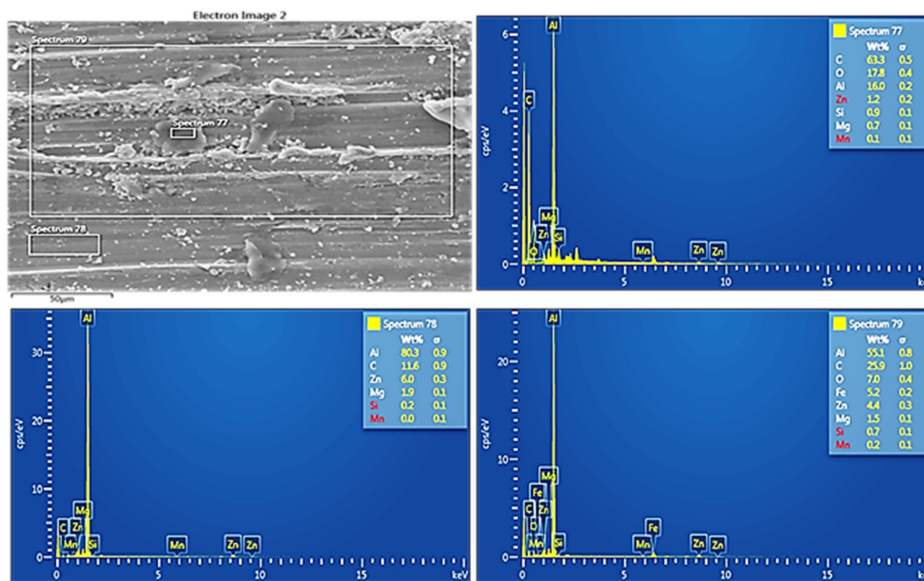


Figure 16. SEM EDX analysis on wear track of the run S-10 Al 7075-SiC/Gr sample.

As illustrated in Figure 16, the somewhat dark uniform region supports the existence of a thin graphitic tribofilm since the spectrum78 reveals the presence of C close to the aluminum alloy. The spectrum79, which finally covered the whole track surface within its view, confirmed the presence of SiC/Gr reinforcement and small amounts of steel disc particles as ferrous (Fe) elements. The SiC particles and Graphite flakes forming the mechanically mixed layer over the run S-10 sample surface have been confirmed through the SEM mapping analysis as shown in Figure 17. The dark black colored flakes of graphite have covered the large surface area on the wear tracks. These spread graphite layers act as a solid lubricating medium that subsequently reduces the mating surfaces' wear rate.

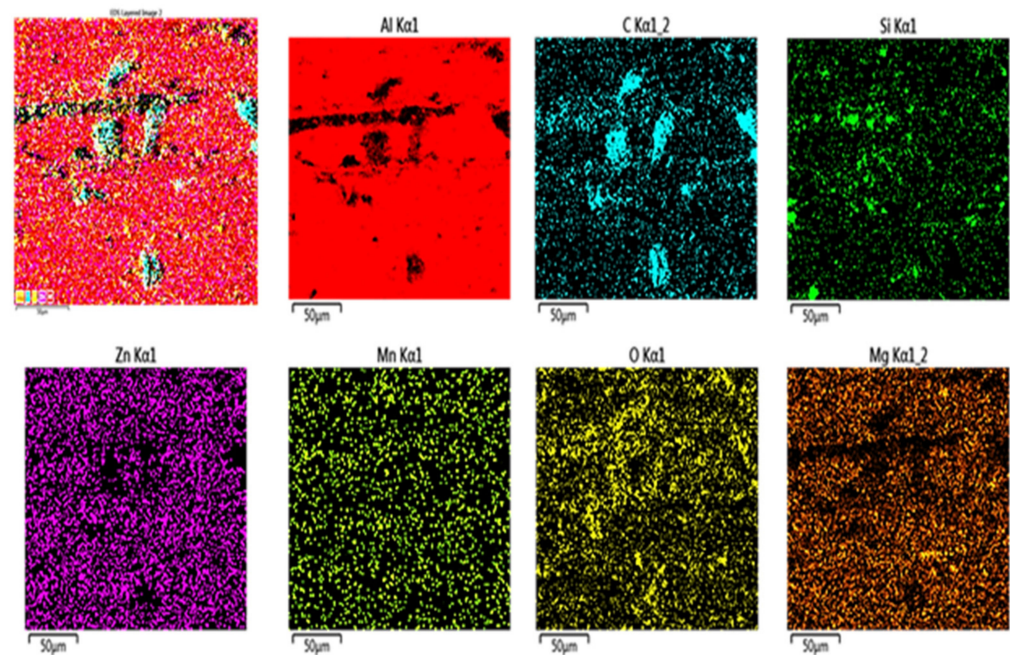


Figure 17. SEM mapping analysis on the wear track of the S-10 Al 7075-SiC/Gr sample.

The surface composites with a high-volume percentage of reinforcements exhibit pulling out phenomenon as a result of low interfacial bonding with the base alloy. As seen in Figure 18, the S-24 wear track exhibits such particles pulling out as a consequence of powder agglomeration and a lack of interfacial bonding with the base alloy, leading to a greater wear rate. Due to the existence of these hard reinforcing particles that have been torn out, the wear process has altered from adhesion to abrasion. The surface fatigue tendency has been increased and the micron sized craters have been observed due to particles pull out as shown in Figure 18b. The pre-fatigue conditions bulging is observed as shown in Figure 18d. The parallel grooves due to abrasion and delaminated layers are also observed on the surface as shown in Figure 18c. So the surface wear has turned higher with abrasion, fatigue and delamination prone zones on this heavily reinforced, loosely particles bonded composite S-24. On other side, in case of the S-10 composite sample, the graphitized-SiC reinforcements resist wear prior to reaching high microhardness and form lubricative tribofilm owing to graphitic flakes between mating surfaces due to homogeneous distribution and strong interfacial bonding with the base alloy. As a result, the S-10 composite sample had a lower wear rate than the S-24 composite sample.

The experimental validation test, i.e., confirmation test sample, processed with parameters of tool rotation-1250 rpm, tool traverse-40 mm/min, hybrid ratio-90:10 and vol. percent.-12 have been tested for wear analysis. The wear tracks have been observed as shown in Figure 19 and were also analyzed through EDX and mapping. The elemental analysis results are shown in Figure 20. In this sample, the abrasive wear tracks are clearly visible with some delamination sites. The adhesive wear look thoroughly absent. The fatigue and fretting wear indications are also not present as shown in Figure 19a–d micrographs. Thus, it can be concluded that the encapsulation of graphitized SiC reinforcement has successfully overcome the fretting fatigue behavior. The SiC particles have acted as the load-bearing elements. They are supported with the graphite tribolayers, making the surface-to-surface contact smooth, thus avoiding any further exploitations of the dendritic α -phase base aluminum alloy. The SiC particles and graphite flakes entrapped can be observed over the surface of wear tracks.

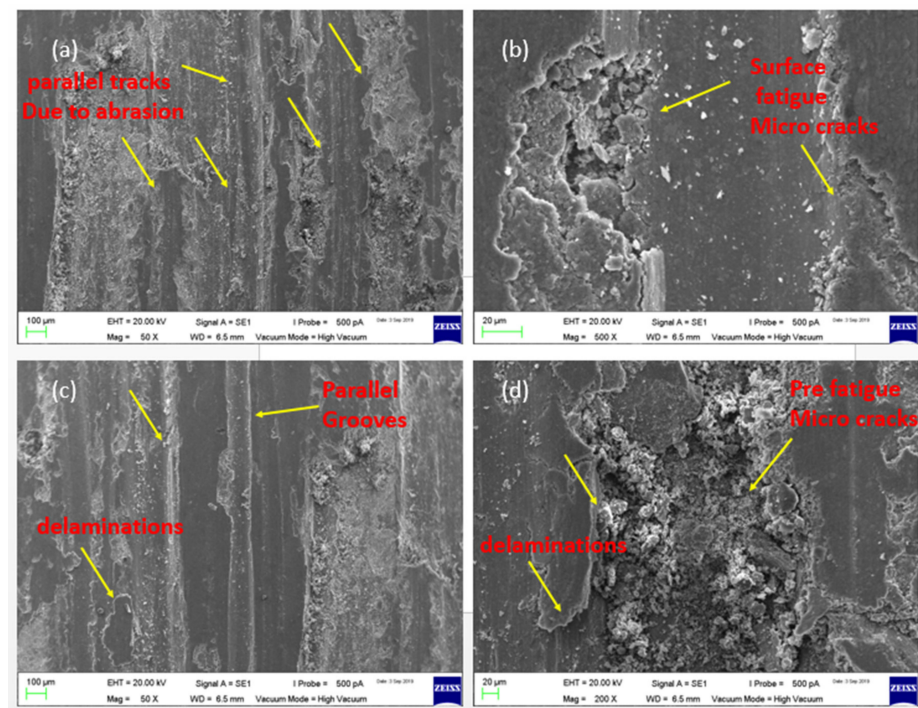


Figure 18. Wear tracks on the run S-24 surface composite indicates (a) parallel tracks due to abrasion (50× magnification) (b) surface fatigue micro cracks (500× magnification) (c) delamination (50× magnification) (d) pre-fatigue zones (200× magnification).

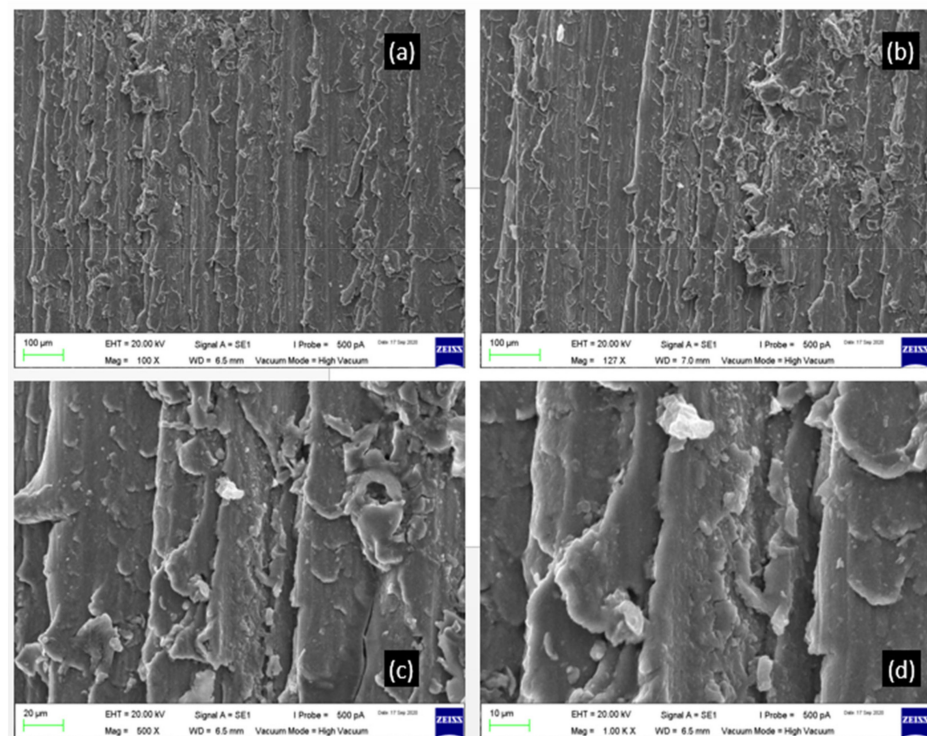


Figure 19. Wear tracks of Al 7075-SiC/Gr confirmation test sample with magnification (a) 100× (b) 127× (c) 500× and (d) 1000×.

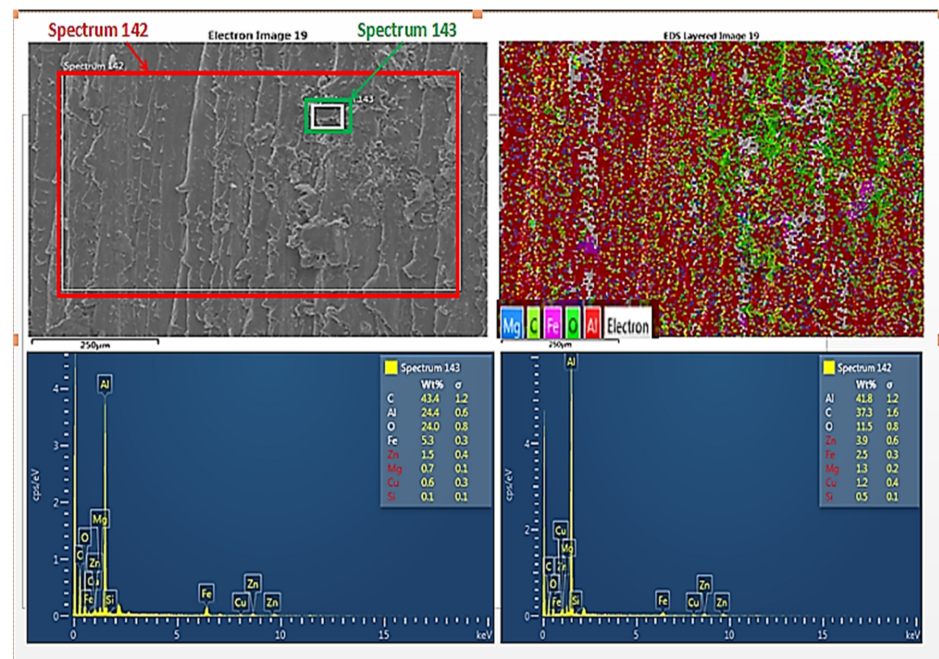


Figure 20. Elemental analysis of Al 7075-SiC/Gr confirmation test wear tracks.

The wear tracks elemental analysis indicates that the wear track is filled with SiC/graphite reinforcement particles, ferrous disk debris particulates, and certain oxides formed with the alloying elements, mainly Zn oxides. The EDX table shows that carbon C- 37 wt% and oxygen O- 11 wt% are present over the surface next to the parent metal Al- 41 wt% for the spectrum 142. The small window that focuses on the dark particulates regions indicates that graphite-exfoliated nanolayers spread along with the oxides formed. The carbon C-43.4% and oxygen O-24% and the parent metal α -phase aluminum Al-24 wt% are detected in spectrum 143. This indicates that the graphite layers along with the SiC nanoparticles have well-encapsulated insides, have spread over the surface, and have been trapped between wear tracks to act as mechanically mixed layers. These tribolayers are responsible for the resultant change in the wear rate of the composite sample. The Al-Fe-O and ZnO formation over the surface is a common phenomenon during wear. The ZnO also is observed in the XRD analysis of the microstructure. The main alloying elements in the form of precipitates gets reacted with atmospheric oxygen during increased temperature environments dry sliding repetitive actions. The oxide films also indicate that the hard isomorphous precipitates have resisted the exploitation of base alloy dendritic structure during wear actions.

3.2.2. Wear Debris Analysis of AA7075-SiC/Graphite Composites

The wear debris of AA7075-T6, S-10, and S-24 AA7075-SiC/Gr Composite samples are analyzed using SEM imaging EDX and mapping elemental analysis. The wear debris images of base alloy AA7075-T6 are shown in Figure 21. Their EDX and mapping results are displayed in Figure 22. From the wear debris images, it is observed that there are mainly two shapes of particulates; one is fine spherical morphology particles which came out of the parent metal alloy during dry sliding wear because of fretting fatigue behavior. The surface cracking and nucleation around the hard precipitates result from the fretting fatigue repetitive loadings during dry sliding actions. Once the surface crack propagates, the inherent precipitates along with α -phase dendritic structures break down due to exposure to the surface repetitive loadings. These forms the fine particulate-shaped debris.

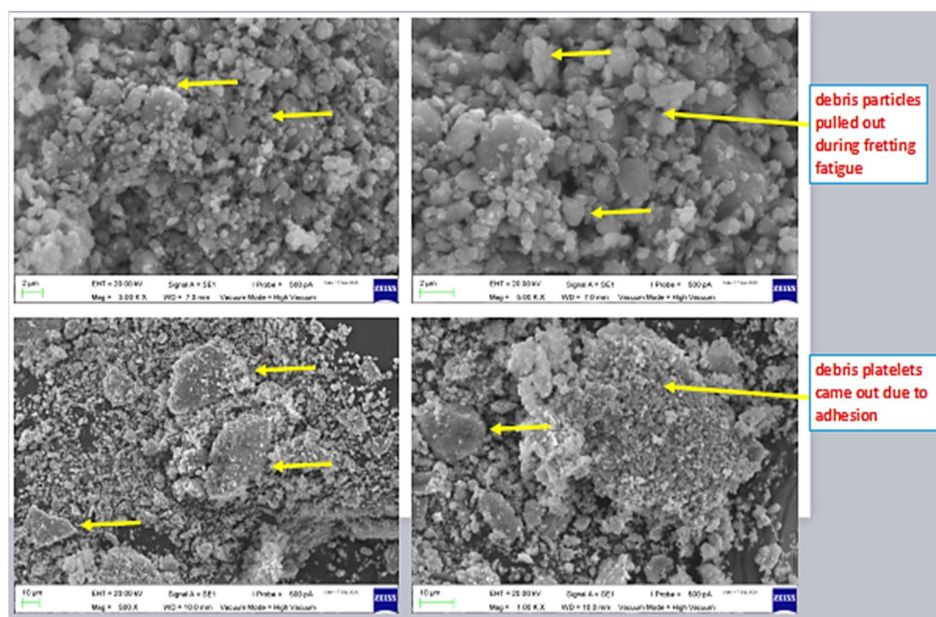


Figure 21. SEM micrographs depicting AA7075-T6 base alloy debris.

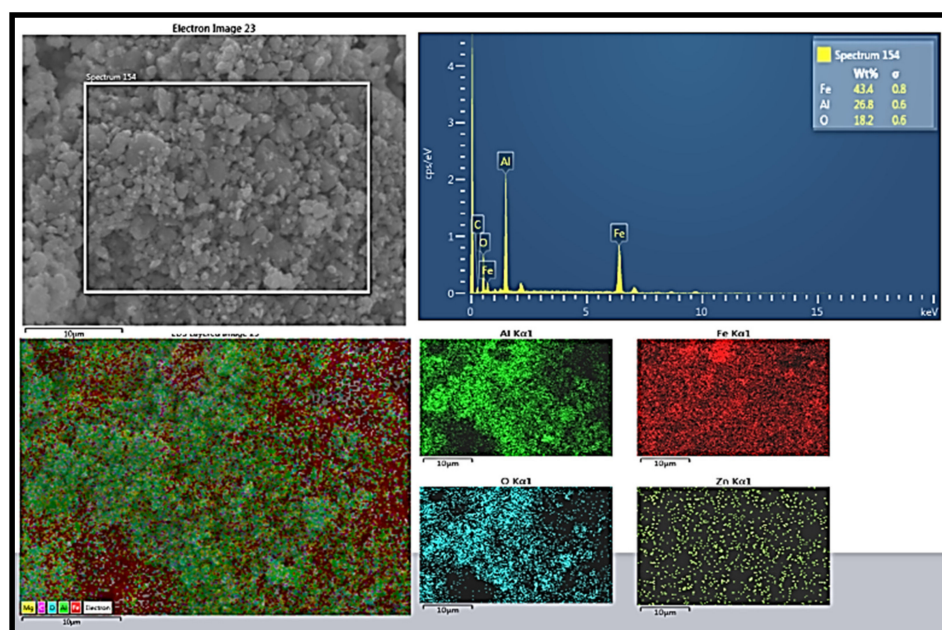


Figure 22. Elemental analysis for the wear debris of AA7075-T6 base alloy.

Secondly, the platelet-like debris are also observed in the imaging; platelets are mainly formed due to detachment during adhesion between the mating surfaces. With the increased temperature at the interface of mating asperities, the plastic flow takes place, which resembles the formation of platelet-like debris and the craters on the base alloy surface once these platelets detach entirely from the surface.

In the EDX and mapping analysis, the debris particles are observed to be a mixture of (Al-Fe-O) oxides. The base aluminum alloy, the ferrous metal alloy disc, and the primary alloying element in the base alloy Zn react with the environmental oxygen to generate these oxides over the surface during the dry sliding actions. The Fe content of 47%, Al content of 27%, and O content of 15% are confirmed in the elemental analysis. The higher Fe content indicates that the hard inherent constituent phases have acted as resisting elements in the wear actions.

The wear debris of the S-24 sample for which the wear rate was the maximum has been analyzed, and the SEM images are shown in Figure 23, and EDX mapping analysis

is shown in Figures 24 and 25. The wear debris show two types of morphologies, mainly the platelets and the spheroids of particulates. As shown in Figure 23a,b the platelets are formed due to the initial fatigue, and then subsequent delamination wear mechanisms. The chip-like structures are pulled out once the cracks are entirely looped around delaminate. The second spheroids of particulates shown in Figure 23c,d are formed due to small fine debris particles from both the pin and disc samples during fatigue continuation. The fine particles, during abrasive wear out actions, agglomerate together and form the spheroid-like structures. The spheroid structures indicate that once the initial asperities have dug out each other's surface in the form of platelets, then the big particles dig-out of platelets or chunks is stopped. Subsequently, only fine debris particles have been observed in the next course of abrasive action because of the high quantity of SiC/Gr agglomeration zones with loose interfaces with the matrix. These fine particles roll between the surfaces and escape out of the zone as the optimized asperities now take full loads between them. The spheroids are formed since the nano-sized SiC/Gr particles tend to agglomerate because of their large surface areas.

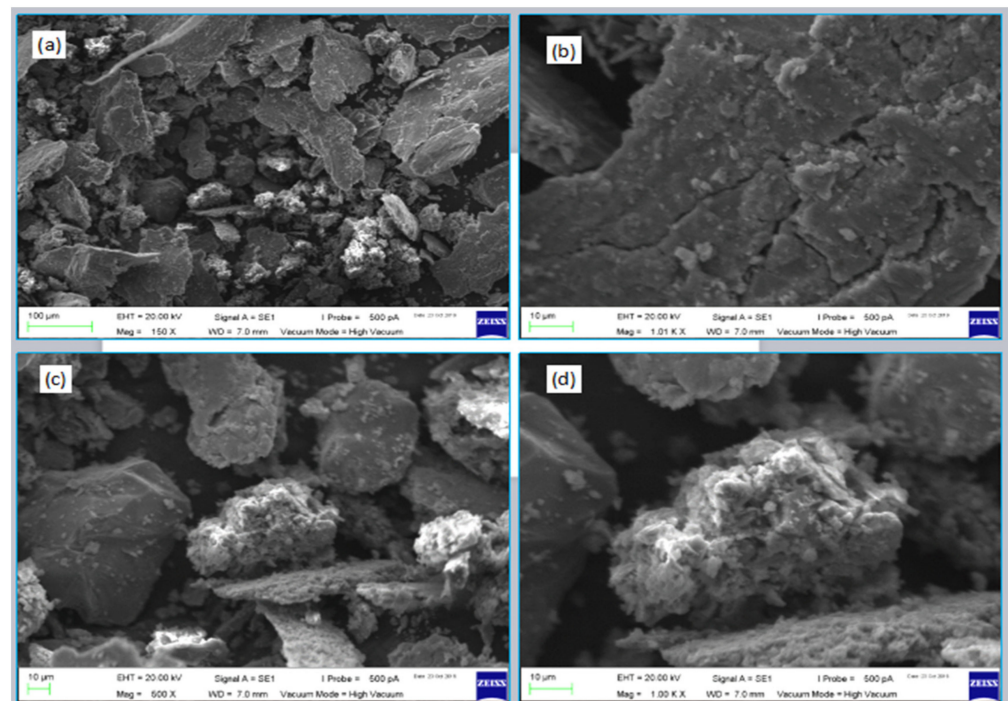


Figure 23. SEM micrographs of wear debris of S-24 AA7075-SiC/Gr composite indicating (a,b) platelets (c,d) particles agglomerated as spheroids.

The SEM EDX analysis shows that the higher Fe content is observed to be 37%, the carbon C-29%, silicon Si- 16.4%, and a small amount of Al-8%. Here, the critical point is that a higher content of SiC and graphite particles have been pulled out during abrasion due to the reinforcement's high-volume percentage. Thus, these reinforcements have initially resisted the wear of the pin. Still, when the repetitive loading continued, the loose interfaces led to the particles pull-out instead of optimizing the firm shaped load-bearing asperities. The initial platelets were generated during the resistance to the mating surface asperities. Then, continuous fine particulates from the pin have been dug out as interfacial bonding was not good. Thus, it is indicated that reinforcement's uniform dispersion with suitable interfaces with matrix material is an essential requirement irrespective of the nature of the reinforcement to be utilized. The latter can be functionalized if the dispersion and interfaces with the α -phase aluminum matrix are good.

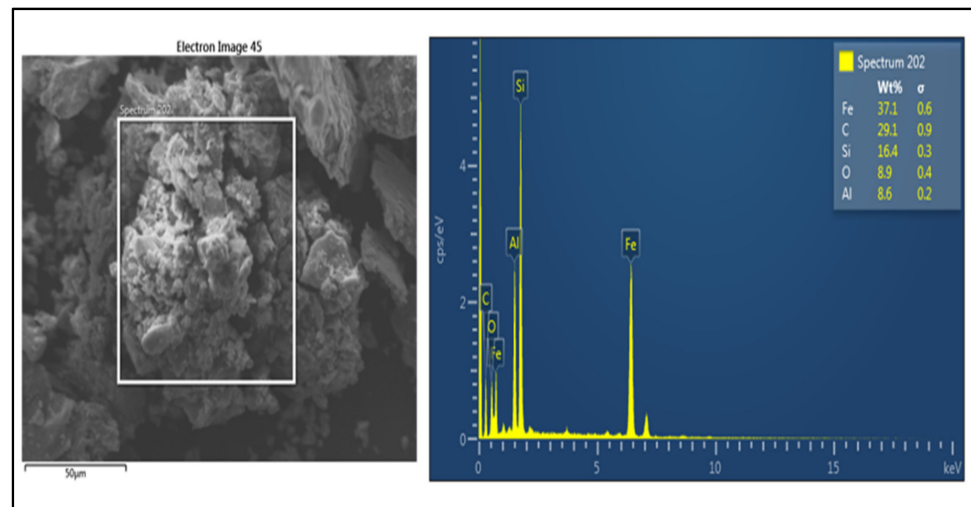


Figure 24. SEM EDX analysis results for S-24 sample wear debris.

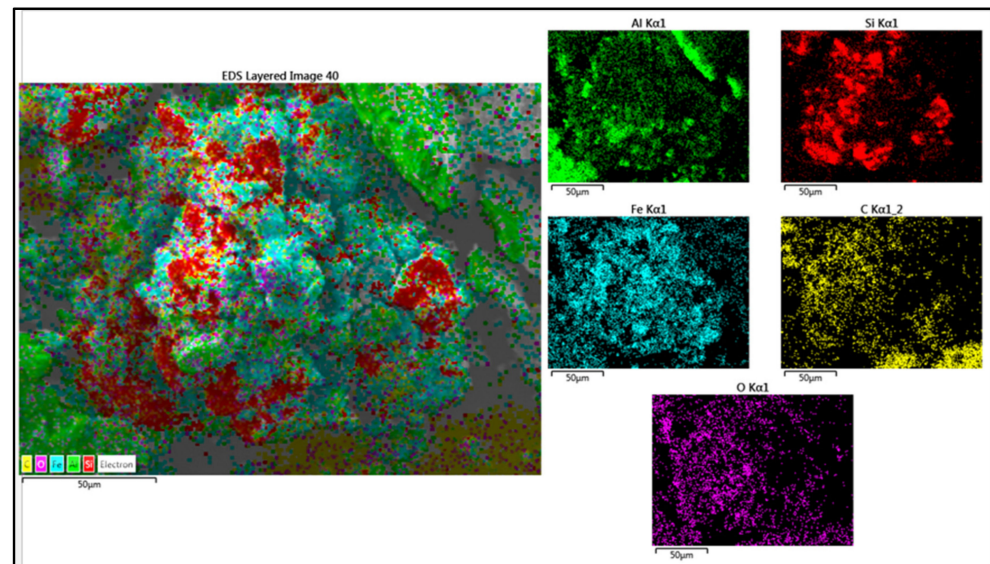


Figure 25. The SEM mapping analysis of the S-24 sample wear debris.

The findings of the S-10 wear sample debris analysis are represented in Figures 26–28. The images of the wear debris generally depict small-sized particulates morphology and in combination with a few giant platelets. Here, in this case, the Fe content has increased in comparison to the last sample, i.e., 38.9%. The Al content is greater, and the Si and C percentages have significantly decreased. This indicates that the SiC and graphite particle pullout has not happened. Instead, the well-bonded graphitized SiC particles have acted as the load-bearing elements and have reduced the wear rate. The initial fatigue action has led to few platelet formations due to the combination of fatigue and delamination. However afterward, once the well-bonded graphitized-SiC particles have exposed and optimized their shapes as the active asperities, the wear rate has decreased significantly. The mechanically mixed layers of graphitized-SiC formed have continuously protected the pin sample area, and only fine debris particles due to abrasion are out. Thus, the large spheroids are not obtained; instead, the fine debris with small sizes is observed.

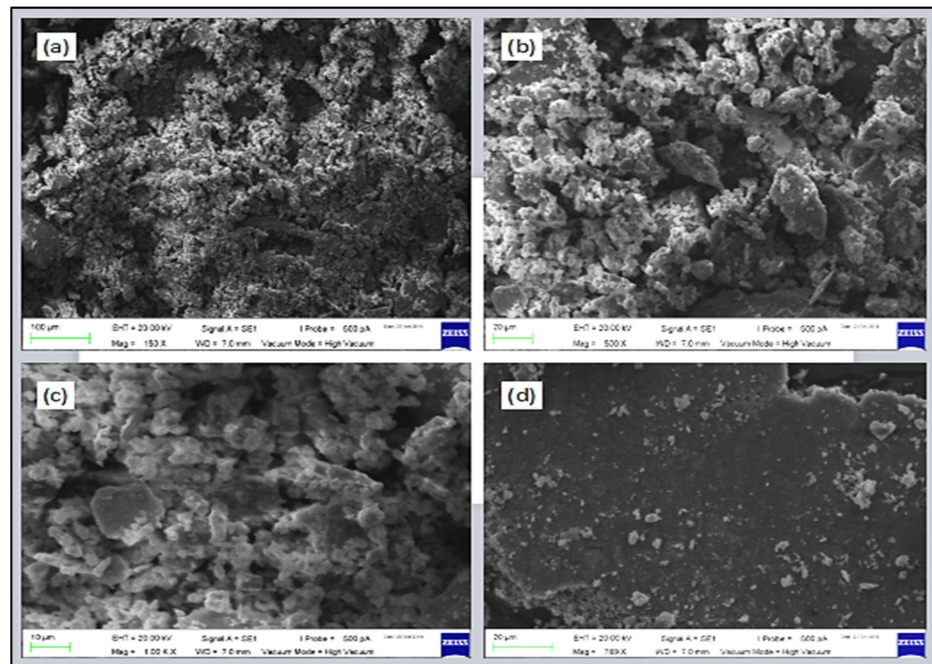


Figure 26. SEM micrographs of wear debris of S-10 AA7075-SiC/Gr composite indicates (a–c) fine particles debris (d) platelets.

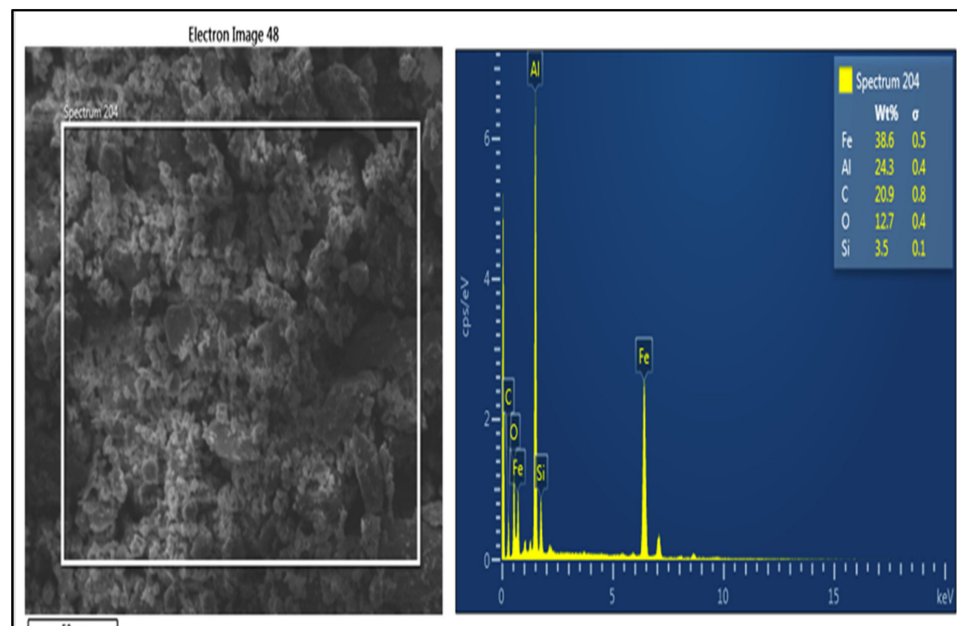


Figure 27. SEM EDX analysis results of S-10 composite wear debris.

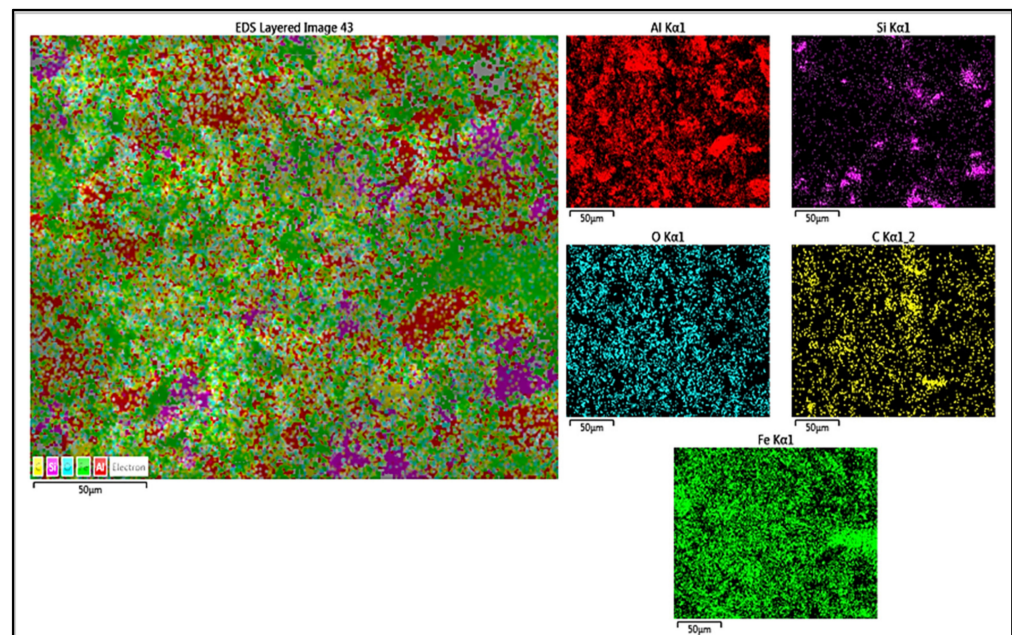


Figure 28. The S-10 AA7075-SiC/Gr composite wear debris mapping results.

4. Conclusions

- The composite fabrication without any macro-level defect was successfully carried out. The wear resistance of the composites was significantly increased (up to 78%) in comparison to the base alloy. The dispersion of reinforcement particles pinned the grain boundaries' expansions during recrystallization, which led to the fine equiaxed grain structures and activated grain size strengthening.
- The wear mechanisms have changed prominently from fretting fatigue with adhesion to abrasion and delamination through reinforcing the graphitized-SiC reinforcements. The wear rate was observed to be a function of graphite content in hybrid ratio with SiC hard particles.
- The graphite exfoliation on the surface of S-10 wear track were confirmed through elemental analysis in EDX as carbon C-43.4% and oxygen O-24% and the parent metal α -phase aluminum Al-24 wt%.
- The adhesion and fretting tendency of base alloys have been confirmed through platelets, spherical size particulates in the wear debris. The high quantity of SiC/Gr agglomeration zones in S-24 led to platelets and loose debris with higher SiC-graphite content in the debris.
- For the most wear resistant S-10 composite wear debris has the maximum Fe content than S-24 and base alloy, i.e., 38.9%. This confirmed that well dispersed SiC-graphite have acted as load-bearing asperities. The SiC particles surrounded with exfoliated graphite layers have acted as load-bearing elements on the surface exposed during dry sliding, and graphite layers further produced the tribofilm to reduce the wear rate.

Author Contributions: Conceptualization, N.A.P. and S.R.P.; methodology, N.A.P. and S.R.P.; software, N.A.P.; validation, N.A.P. and S.R.P.; formal analysis, N.A.P., S.R.P. and R.V.M.; investigation, N.A.P., S.R.P. and R.V.M.; resources, S.R.P.; data curation, N.A.P., S.R.P. and R.V.M.; writing—original draft preparation, N.A.P.; writing—review and editing, N.A.P., S.R.P. and R.V.M.; supervision, S.R.P.; project administration, S.R.P.; funding acquisition, S.R.P. All authors have read and agreed to the published version of the manuscript.

Funding: This research received no external funding.

Acknowledgments: The work was supported by the Institute of Transport Infrastructure, Universiti Teknologi PETRONAS, Malaysia.

Conflicts of Interest: The authors declare no conflict of interest.

References

1. Rajan, R.; Kah, P.; Mvola, B.; Martikainen, J. Trends in aluminium alloy development and their joining methods. *Rev. Adv. Mater. Sci.* **2016**, *44*, 383–397.
2. Khan, N.Z.; Siddiquee, A.N.; Khan, Z.A.; Mukhopadhyay, A.K. Mechanical and microstructural behavior of friction stir welded similar and dissimilar sheets of AA2219 and AA7475 aluminium alloys. *J. Alloys Compd.* **2017**, *695*, 2902–2908. [[CrossRef](#)]
3. Mathers, G. Material standards, designations and alloys. In *The Welding of Aluminium and Its Alloys*, 1st ed.; Woodhead Publishing: Cambridge, UK, 2002. [[CrossRef](#)]
4. Dong, H. Surface Engineering of Light Alloys: Aluminium, Magnesium and Titanium Alloys. Available online: <https://books.google.com.my/books?id=r9c2EAAAQBAJ> (accessed on 9 August 2022).
5. Evans, A.; Marchi, C.S.; Mortensen, A. *Metal Matrix Composites in Industry*; Springer: New York, NY, USA, 2003.
6. Wang, Y.; Zhang, X.; Zeng, G.; Li, F. In situ production of Fe-VC and Fe-TiC surface composites by cast-sintering. *Compos. Part A Appl. Sci. Manuf.* **2001**, *32*, 281–286. [[CrossRef](#)]
7. Wang, Y.; Zhang, X.; Zeng, G.; Li, F. Cast sinter technique for producing iron base surface composites. *Mater. Des.* **2000**, *21*, 447–452. [[CrossRef](#)]
8. Gui, M.; Kang, S.B.; Euh, K. Influence of spraying conditions on microstructures of Al-SiCp composites by plasma spraying. *Metall. Mater. Trans. A Phys. Metall. Mater. Sci.* **2005**, *36*, 2471–2480. [[CrossRef](#)]
9. Hu, C.; Baker, T.N. A new aluminium silicon carbide formed in laser processing. *J. Mater. Sci.* **1997**, *32*, 5047–5051. [[CrossRef](#)]
10. Pantelis, D.; Tissandier, A.; Manolatos, P.; Ponthiaux, P. Formation of wear resistant Al-SiC surface composite by laser melt-particle injection process. *Mater. Sci. Technol.* **1995**, *11*, 299–303. [[CrossRef](#)]
11. Hu, C.; Xin, H.; Baker, T.N. Formation of continuous surface Al-SiCp metal matrix composite by overlapping laser tracks on AA6061 alloy. *Mater. Sci. Technol.* **1996**, *12*, 227–232. [[CrossRef](#)]
12. Katipelli, L.R.; Dahotre, N.B. Mechanism of high temperature oxidation of laser surface engineered TiC/Al alloy “composite” coating on 6061 aluminium alloy. *Mater. Sci. Technol.* **2001**, *17*, 1061–1068. [[CrossRef](#)]
13. Bakshi, S.R.; Singh, V.; Balani, K.; McCartney, D.G.; Seal, S.; Agarwal, A. Carbon nanotube reinforced aluminum composite coating via cold spraying. *Surf. Coat. Technol.* **2008**, *202*, 5162–5169. [[CrossRef](#)]
14. Kumar, R.; Dhiman, S. A study of sliding wear behaviors of Al-7075 alloy and Al-7075 hybrid composite by response surface methodology analysis. *Mater. Des.* **2013**, *50*, 351–359. [[CrossRef](#)]
15. Choo, S.H.; Lee, S.; Kwon, S.J. Effect of flux addition on the microstructure and hardness of TiC-reinforced ferrous surface composite layers fabricated by high-energy electron beam irradiation. *Metall. Mater. Trans. A Phys. Metall. Mater. Sci.* **1999**, *30*, 3131–3141. [[CrossRef](#)]
16. Mishra, R.S.; Mahoney, M.W.; McFadden, S.X.; Mara, N.A.; Mukherjee, A.K. High strain rate superplasticity in a friction stir processed 7075 Al alloy. *Scr. Mater.* **1999**, *42*, 163–168. [[CrossRef](#)]
17. Oza, M.J.; Schell, K.G.; Bucharsky, E.C.; Laha, T.; Roy, S. Developing a hybrid Al-SiC-graphite functionally graded composite material for optimum composition and mechanical properties. *Mater. Sci. Eng. A* **2021**, *805*, 140625. [[CrossRef](#)]
18. Ande, R.; Gulati, P.; Shukla, D.K.; Dhingra, H. Microstructural and Wear Characteristics of Friction Stir Processed Al-7075/SiC Reinforced Aluminium Composite. *Mater. Today Proc.* **2019**, *18*, 4092–4101. [[CrossRef](#)]
19. Dhayalan, R.; Kalaiselvan, K.; Sathiskumar, R. Characterization of AA6063/SiC-Gr Surface Composites Produced by FSP Technique. *Proc. Eng.* **2014**, *97*, 625–631. [[CrossRef](#)]
20. Sharma, A.; Sharma, V.M.; Mewar, S.; Pal, S.K.; Paul, J. Friction stir processing of Al6061-SiC-graphite hybrid surface composites. *Mater. Manuf. Proc.* **2018**, *33*, 795–804. [[CrossRef](#)]
21. Sharma, A.; Narsimhachary, D.; Sharma, V.M.; Sahoo, B.; Paul, J. Surface modification of Al6061-SiC surface composite through impregnation of graphene, graphite & carbon nanotubes via FSP: A tribological study. *Surf. Coat. Technol.* **2019**, *368*, 175–191.
22. Rambabu, P.; Prasad, N.E.; Kutumbarao, V.V.; Wanhill, R.J.H. *Aluminium Alloys for Aerospace Applications*; Springer: Singapore, 2017; pp. 29–52.
23. Bertolini, R.; Simonetto, E.; Pezzato, L.; Fabrizi, A.; Ghiotti, A.; Bruschi, S. Mechanical and corrosion resistance properties of AA7075-T6 sub-zero formed sheets. *Int. J. Adv. Manuf. Technol.* **2021**, *115*, 2801–2824. [[CrossRef](#)]
24. Dursun, T.; Soutis, C. Recent developments in advanced aircraft aluminium alloys. *Mater. Des.* **2014**, *56*, 862–871. [[CrossRef](#)]
25. Oskouei, R.H.; Barati, M.R.; Ibrahim, R.N. Surface Characterizations of Fretting Fatigue Damage in Aluminum Alloy 7075-T6 Clamped Joints: The Beneficial Role of Ni-P Coatings. *Materials* **2016**, *9*, 141. [[CrossRef](#)] [[PubMed](#)]
26. Mishra, A. Dry Sliding Wear of Wrought Al-Alloys. *IJMERR* **2014**, *3*. Available online: <http://www.ijmerr.com/show-124-494-1.html> (accessed on 10 August 2022).
27. Majzoobi, G.H.; Nemati, J.; Rooz, A.J.N.; Farrahi, G.H. Modification of fretting fatigue behavior of AL7075-T6 alloy by the application of titanium coating using IBED technique and shot peening. *Tribol. Int.* **2009**, *42*, 121–129. [[CrossRef](#)]
28. Raja, K.; Sekar, V.S.C.; Kumar, V.V.; Ramkumar, T.; Ganeshan, P. Microstructure Characterization and Performance Evaluation on AA7075 Metal Matrix Composites Using RSM Technique. *Arab. J. Sci. Eng.* **2020**, *45*, 9481–9495. [[CrossRef](#)]
29. Patil, N.A.; Pedapati, S.R.; Mamat, O.; Lubis, A.M.H.S. Optimization of Friction Stir Process Parameters for Enhancement in Surface Properties of Al 7075-SiC/Gr Hybrid Surface Composites. *Coatings* **2019**, *9*, 830. [[CrossRef](#)]

30. Patil, N.A.; Pedapati, S.R.; Mamat, O.; Lubis, A.M.H.S. Morphological characterization, statistical modeling and wear behavior of AA7075-Titanium Carbide-Graphite surface composites via Friction stir processing. *J. Mater. Res. Technol.* **2021**, *11*, 2160–2180. [[CrossRef](#)]
31. ASTM G99–17 Standard Test Method for Wear Testing with a Pin-on-Disk Apparatus. Available online: <https://www.astm.org/standards/g99> (accessed on 11 August 2022).
32. Singh, S.; Rathi, K.; Pal, K. Synthesis, characterization of graphene oxide wrapped silicon carbide for excellent mechanical and damping performance for aerospace application. *J. Alloys Compd.* **2018**, *740*, 436–445. [[CrossRef](#)]
33. Dixit, S.; Mahata, A.; Mahapatra, D.R.; Kailas, S.V.; Chattopadhyay, K. Multi-layer graphene reinforced aluminum—Manufacturing of high strength composite by friction stir alloying. *Compos. Part B Eng.* **2018**, *136*, 63–71. [[CrossRef](#)]
34. Hull, A.W. A New Method of X-Ray Crystal Analysis. *Powder Diffr.* **1992**, *7*, 13–27. [[CrossRef](#)]
35. Ramsdell, L.S.; Kohn, J.A. Developments in silicon carbide research. *Acta Crystallogr.* **1952**, *5*, 215–224. [[CrossRef](#)]
36. Bundy, F.P.; Kasper, J.S. Hexagonal diamond—A new form of carbon. *J. Chem. Phys.* **1967**, *46*, 3437–3446. [[CrossRef](#)]